

Evaluating clay stiffness effects on offshore pile running with the Coupled Eulerian Lagrangian Method

Dyson, A. P.; Tolooiyan, A.; Gavin, K.

10.1016/j.compgeo.2025.107185

Publication date

Document Version Final published version

Published in

Computers and Geotechnics

Citation (APA)
Dyson, A. P., Tolooiyan, A., & Gavin, K. (2025). Evaluating clay stiffness effects on offshore pile running with the Coupled Eulerian Lagrangian Method. *Computers and Geotechnics*, *183*, Article 107185. https://doi.org/10.1016/j.compgeo.2025.107185

Important note

To cite this publication, please use the final published version (if applicable). Please check the document version above.

Copyright

Other than for strictly personal use, it is not permitted to download, forward or distribute the text or part of it, without the consent of the author(s) and/or copyright holder(s), unless the work is under an open content license such as Creative Commons.

Please contact us and provide details if you believe this document breaches copyrights. We will remove access to the work immediately and investigate your claim.

ELSEVIER

Contents lists available at ScienceDirect

Computers and Geotechnics

journal homepage: www.elsevier.com/locate/compgeo



Research Paper

Evaluating clay stiffness effects on offshore pile running with the Coupled Eulerian Lagrangian Method

A.P. Dyson^a, A. Tolooiyan^{a,*}, K. Gavin^b

- a Computational Engineering for Sustainability Lab (CES-Lab), School of Engineering, University of Tasmania, Hobart, TAS 7001, Australia
- ^b Faculty of Civil Engineering and Geosciences, Delft University of Technology, Delft, the Netherlands

ARTICLE INFO

Keywords: Pile running Coupled Eulerian Lagrangian Pile free-fall Large deformation Heave Rigidity index

ABSTRACT

Driven pipe piles are used extensively in coastal and offshore projects. Traditionally piles with diameters of 2–3 m were common in the offshore wind industry, however the diameter of monopiles to support a 10 MW wind turbine is more commonly 10 m. Offshore wind projects are being developed at sites with very low seabed strengths and pipe pile weights are increasing significantly. Self-weight penetration occurs when the pile is first placed on the seabed. A combination of low strength seabed conditions and increased pile self-weight leads to the risk of pile run (uncontrolled self-weight penetration) during installation at some sites. Predicting pile run risk, run velocities and penetration depths is challenging due to inherent rate effects and the large strains involved. While rapid penetration processes can be considered using both analytic methods and Large Deformation Finite Element simulations, the role of soil rigidity is seldom taken into account, despite known implications from static pile assessments. This study uses large deformation simulation with the Coupled Eulerian Lagrangian method to simulate the pile running process for five well-studied fine-grained soils with varying elastic stiffnesses. Results are compared with analytic methods, highlighting the limitations of current predictive techniques in terms of both the end tip and shaft resistance. As a corollary, a linear trend for the final penetration depth with respect to the logarithm of the soil rigidity index is incorporated in an existing analytic code based on results obtained from large deformation simulations.

1. Introduction

During offshore installation of a pile, rapid, uncontrolled penetration can occur when the soil resistance cannot support the pile dead weight, which can be in excess of 1,000 tonnes. Free-fall, high-velocity descent can damage the driving hammer, while sling failures can result in hammer loss and high snap loads. Pile running is primarily attributed to (1) the presence of layered soils where underlying materials promote punch-through (Zhao et al., 2023), (2) the reduction of shaft resistance as a result of particle breakage (commonly in carbonate soils) (Senders et al., 2013) and (3) clays with insufficient end bearing resistance to provide support. Dover and Richardson (2007) report 26 pile running events at the Richmond Sand Rafael that were attributed to clay with insufficient end bearing. Yan et al. (2015) noted that the presence of unexpected soft clay layers was the primary cause of a set of uncontrolled pile penetrations observed in the South China Sea, where multiple 158-metre piles exhibited uncontrolled penetration in excess of 20 m in depth. Additional pile running events in soft clays were noted in

locations including Shanghai harbour (Shengchang & Shaolin, 2011) and Western India (Tian & Cassidy, 2022).

Current analytical methods for calculating the free-fall pile velocities and total penetration depths are based on the governing equations of motion, whereby resistive and driving forces determine pile acceleration. During running, the sum of the end bearing capacity and shaft resistance is less than the driving force due to the pile deadweight and force provided by the hammer impact. Sun et al. (2016) developed a procedure to calculate velocities and penetration depths during driving, similar to methods used for dynamic plate anchor penetration (O'Loughlin et al., 2016) and free-fall penetrometers (Chow et al., 2023). Expanding the method, (Sun et al., 2022) considered pile run in the South China Sea, showing good agreement with field observations. Kong et al. (2019) highlighted the effects of various skin friction reduction factors to develop piecewise functions for dynamic friction resistance in sand and clay. A limitation of these analytic methods is that several a-priori assumptions are required, notably the selection of an appropriate ratio of internal to external shaft friction. Based on the bearing capacity calculations implemented, the soil is also considered as

E-mail address: Ali.Tolooiyan@utas.edu.au (A. Tolooiyan).

^{*} Corresponding author.

Nomenclature		m_p	hammer weight [kg]	
		N_c , N_q	bearing capacity factors [-]	
A_{cross}	cross-sectional area of the pile [m ²]	q_t	tip resistance [Pa]	
g	gravity [m/s²]	r	inner radius [m]	
D	outer diameter of the pile [m]	R	outer radius [m]	
F_b	soil buoyancy from seawater [MN]	\mathcal{S}_t	sensitivity of clay [-]	
F_{bear}	end bearing resistance [MN]	s_u	undrained shear strength [kPa]	
F_d	inertial drag resistance [MN]	t	wall thickness [m]	
F_s	skin friction [MN]	ν	pile velocity [m/s]	
F_{total}	total resistance [MN]	$ u_0$	instantaneous velocity of pile and hammer [m/s]	
G	soil rigidity index [-]	z_{tip}	soil depth [m]	
G_{pile}	total gravitation forces of the pile and hammer [MN]	α	adhesion factor [-]	
I_r	rigidity index [-]	γ	soil unit weight [N/m ³]	
K_0	coefficient of at rest earth pressure [-]	σ'_{v0}	vertical effective stress [Pa]	
L	pile length [m]	70	- -	
m_h	ram weight [kg]			

incompressible. Large Deformation Finite Element (LDFE) methods present an alternative for simulating uncontrolled pile penetration, plugging and soil flow. The Coupled Eulerian Lagrangian method (CEL) is widely used for 'large-strain' geotechnical simulation of a variety of onshore and offshore applications ranging from spudcan installation (Tolooiyan et al., 2024) to landslide runout (Sha et al., 2023) and laboratory shear tests (Tatnell et al., 2021). In the case of pile running, Zhao et al. (2023) used CEL to model pile descent in layered soils to understand soil flow across soil boundary layers. Tian and Cassidy (2022) presented three known cases of pile running with CEL, comparing inner and after shaft resistance profiles, while noting some discrepancies with the bearing resistance obtained from analytic calculations.

Due to their inherent stress-strain-based formulation, LDFE methods allow for the effects of soil stiffness, E and compressibility to be assessed. While the role of stiffness in analytical methods is neglected, the impacts of foundation stiffness and compressibility in static bearing capacity analyses are well understood. When considering non-linear materials, Randolph et al. (1994) noted that the end-bearing capacity of piles is a function of both soil strength and rigidity index (i.e. the ratio of stiffness to strength). Poulos et al. (2002) noted that the stiffness of soil surrounding the pile shaft and immediately beneath the pile tip strongly influences the settlement of single piles and small pile groups. Estimation of soil stiffness for foundations is discussed at length by Poulos (1994) and Mayne (1995). Vesić (1973) proposed a set of soil compressibility factors for cohesive soils based on cavity expansion theory to accommodate volume changes in the plastic zone, for the purpose of bearing capacity calculations that account for stiffness. Analogous to cone penetration, a set of stiffness-dependent CPT cone factors (N_k) have been presented by Baligh et al. (1980), Teh and Houlsby (1991) and Vesić (1972). Resultingly, Yu and Mitchell (1998) compiled values of N_k ranging from 8.3 to 18.0, for Rigidity Index (I_r) of 50 to 400, respectively. The extent of plastic zone formation for deep penetration is also dependent on I_r , as shown by Fallah et al. (2016) and Lu et al. (2004). Zhou et al. (2024) considered the effects of elastic stiffness on the end bearing resistance of various piles and bucket foundations, while also focusing on the size of the plastic zone. Despite known stiffness effects for static pile bearing capacities and dynamic cone penetration, existing pile run analyses focus primarily on shear strength as the governing factor in both the penetration depth and velocity.

This research presents five well-researched fine-grained soils and their susceptibility to free-fall to identify stiffness-dependencies in uncontrolled pile penetration. Trends in velocity and displacement are presented using LDFE simulation and are compared with a modified analytic pile running method based on rigidity index. Further features specific to LDFE simulation, namely time-dependent heave within the

pipe pile and the shape of the plastic zone surrounding the pile, are presented.

2. Existing methods for pile running analysis

A brief description of the governing equations based on soil resistive and driving forces based on the analytic method proposed by (Sun et al., 2016) are provided. Following Newton's Second Law of Motion, the soil-pile-hammer equilibrium is obtained by

$$\frac{1}{2}\left(m_p + m_h\right)\frac{d^2z_{tip}}{dt^2} = G_{pile} - F_s - F_{bear} - F_b - F_d \tag{1}$$

where, m_p is the pile mass; m_h is the hammer mass; z_{tip} is the position of the pile tip; G_{pile} is the force of the pile hammer due to gravity; F_s is the pile sleeve resistance; F_{bear} is the end-bearing resistance; F_b is the buoyant weight of the displaced soil; and F_d is the inertial drag force. Based on Equation (1), velocities are determined at discrete calculation steps j-1 and j, at which the pile-hammer system displaces a distance ΔS

$$\frac{1}{2}\left(m_h + m_p\right)\left(v_j^2 - v_{j-1}^2\right) = (G - F_s - F_{bear} - F_b)\Delta S \tag{2}$$

The end-bearing resistance and shaft friction are calculated based on the American Petroleum Institute (API) Guideline RP 2A-WSD (API, 2020) for axially loaded piles. The side friction, F_s , is calculated as the sum of the friction on the inner and outer pile surfaces

$$F_s = \int_0^\infty f_s(z)(1+\beta)\pi Ddz \tag{3}$$

where, f_s represents the unit skin friction; β is the ratio of inner and outer skin friction, typically ranging from 0 to 0.5 (Dover & Davidson, 2007); and D is the outer diameter of the pile. Sun et al. (2016) back-calculated appropriate values for β based on site conditions for a pile running case in the South China Sea, observing a ratio closer to 0.4. For pipe piles installed in clay soils, the total stress α -method is used, where

$$f_s(\mathbf{z}) = \alpha \mathbf{s}_u \tag{4}$$

where s_u is the undrained shear strength; with α defined as follows

$$\alpha = \frac{1}{2} \left(\frac{s_u}{\sigma_{v_o}} \right)^{-0.5}, \frac{s_u}{\sigma_{v_o}} \le 1$$
 (5a)

$$\alpha = \frac{1}{2} \left(\frac{s_u}{\sigma'_{v_o}} \right)^{-0.25}, \frac{s_u}{\sigma'_{v_o}} \ge 1$$
 (5b)

 Table 1

 Numerical model input parameters (Tresca soil model).

Soil	Elastic Modulus — E ₃₀ , E ₄₀ , E ₅₀ (MPa)	Peak deviatoric stress (kPa)	Reference
Wenzhou clay Coode Island silt	2.8, 3.5, 5.2 36.8, 23.2, 16.0	70 70	Wang et al. (2013) Jamali et al. (2018a) and Jamali et al. (2018b)
Shanghai clay	11.6, 9.8, 9	82	Hong et al. (2007), Ye and Ye (2016)
Champlain Sea clay	15.0, 14.6, 13.0	101	Liu et al. (2021)
Tiller clay	11.7, 12.8, 13.0	134	D'Ignazio and Länsivaara (2015)

where, σ'_{ν_o} is the effective overburden stress. For sand layers, f_s is calculated using the effective stress β -method

$$f_s(z) = \beta_s \sigma'_{v0} = K_0 \, \sigma'_{v0} tan\delta \tag{6}$$

where, β_s is a function of the coefficient of lateral earth pressure (K₀) and soil-pile friction angle is given by δ . Soil buoyancy is considered in the governing equation provided by Eq (1) as follows

$$F_b = (z + h_w)\gamma_w \pi Dt \tag{7}$$

where, h_w is the seawater depth; γ_w is the unit weight of water; and t is the pile thickness. The end-bearing pressure $q_{tip}(z)$ for clay layers is calculated by

$$q_{tip}(z) = N_c s_u = 9s_u \tag{8}$$

While N_c is often assigned a value equal to 9, the bearing capacity factor can range from 6 sensitive normally consolidated clays to over 12 for overconsolidated clays. The end-bearing resistance F_{bear} is determined based on the area A of the pile shoe (defined by an annulus)

$$F_{bear} = q_{tip}A \tag{9}$$

2.1. Bearing capacity analysis based on soil stiffness

Using cavity expansion theory, Menard (1957) derived the limit pressure (p_l) of cylindrical cavities in cohesive soils of the form

$$p_l = s_u N_c + \sigma_h \tag{10}$$

where $N_c = 1 + \ln(I_r)$, such that I_r is the ratio of the shear modulus G with respect to the undrained shear strength. In the case of pile bearing resistance as a result of cavity expansion theory, Vesic (1977) proposed an equation for the end-bearing resistance

$$q_{tip} = cN_c + \sigma_m' N_\sigma \tag{11}$$

where, the mean stress σ_m' at the base of the pile is given by

$$\sigma'_{m} = \frac{1 + 2K_{0}}{3} q_{tip} \tag{12}$$

Both N_c and N_σ are bearing capacity factors based on cohesion and stress. Based on Vesić's theory, N_c in frictionless soil is given by

$$N_c = \frac{4}{3}(\ln I_m + 1) + \frac{\pi}{2} + 1, (\phi = 0)$$
(13)

where I_{rr} is a reduced rigidity index defined as

$$I_{rr} = \frac{I_r}{1 + I_r \varepsilon_r^p} \tag{14}$$

such that ε_{ν}^{p} is the average volumetric strain within the plastic zone beneath the pile tip. In undrained conditions, the reduced rigidity index can be considered as equal to the rigidity index, which for typical clays ranges from 50-500. N_{c} varies from 6.97 to 12.19 for rigidity indices of 10 to 500, respectively, as compared with a condition of $N_{c}=9$ commonly implemented when stiffness is not considered. This range is lower than obtained by rigorous numerical simulation, as noted by Lu et al. (2004), as is shown later.

2.2. Soil description

The mechanical properties of marine clays obtained from element tests are the focus of numerous studies for deepwater foundation design (Lunne & Andersen, 2007; Lunne et al., 2011; Wang et al., 2013). The soft marine clays considered in this research were selected based on their residual shear strength (70 kPa), which are summarised in Table 1. Specific details of the initial tests conducted are provided as a point of reference. At large strains, these soils exhibit comparable shear strengths, while displaying varying behaviour at smaller strains, as

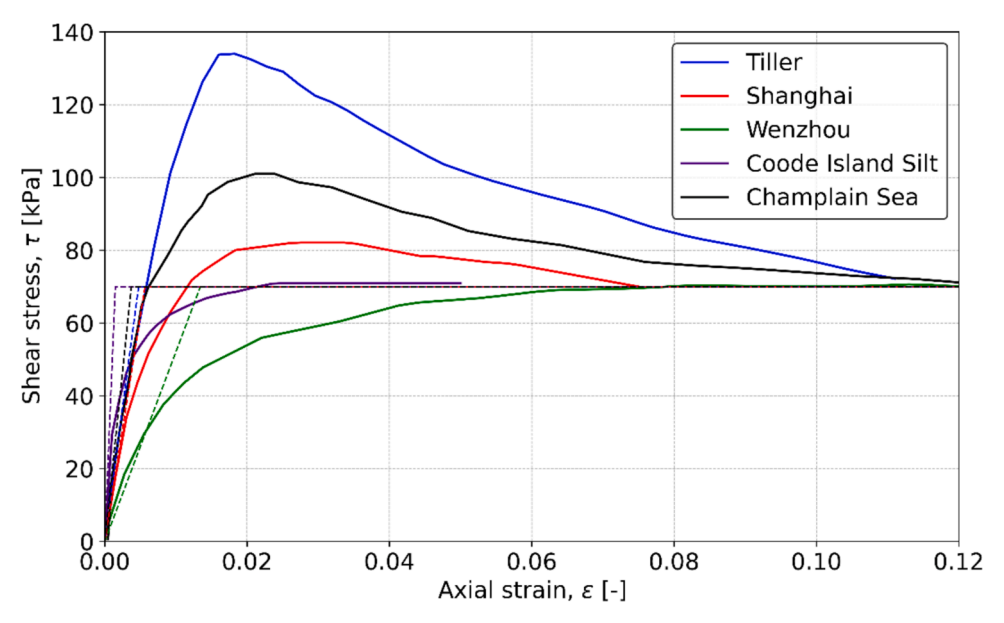


Fig. 1. Comparative stress-strain curves and secant moduli, E_{50} , for five soils considered.

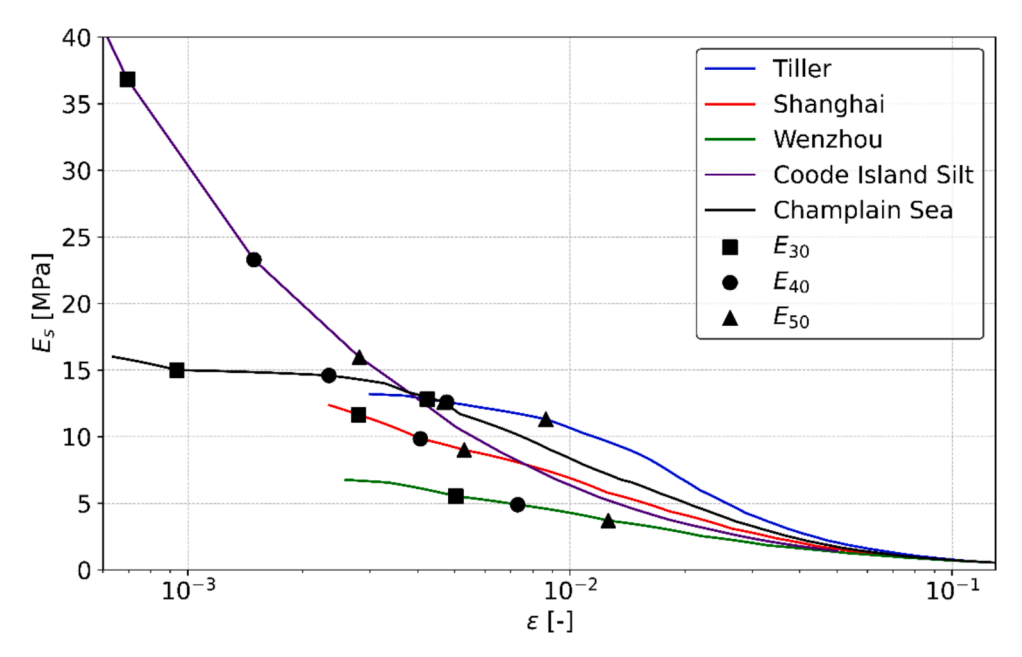


Fig. 2. Secant modulus reduction curves (E_{30} to E_{50} indicated).

indicated by Fig. 1. In this case, the two normally consolidated finegrained soils (Wenzhou and Coode Island Silt) and three lightly overconsolidated clays exhibit relatively low stiffnesses. The constitutive behaviour herein considers each soil as linear elastic perfectly plastic to isolate the effects of soil rigidity impacting pile displacement (and are thus solely based on the elastic modulus). Calculations are carried out assuming shear strength is irrespective of the strain path. As such, the extent of the plastic zone around the tip of piles in free-fall (and the neighbouring elastic zone) is a function of the given soil stiffness. Given each soil exhibits the same undrained shear strength, the sole parameter varying from soil to soil is E, the elastic modulus, thereby limiting changes in pile response purely to the stiffness of the soil. Based on this concept, whereby hardening and softening behaviour is not permissible, the Tresca criteria is suitable for the clays considered, with soil input parameters given in Table 1. The elastic modulus is given based on E_{30} . E_{40} and E_{50} , with Coode Island silt exhibiting significant variation in the stiffness, depending on the strain level considered. Fig. 2 indicates the

range of secant stiffnesses for E_{50} , (the stiffness mobilised when the shear stress is 50 % of the peak shear resistance), with dashed lines indicating the idealised linear elastic perfectly plastic soil model considered. It is evident that both Champlain Sea and Tiller clays show minor sensitivity, with post-peak softening. In the analyses presented herein, linear elastic perfectly plastic behaviour is considered using remoulded shear strengths, as has been accepted in the analytic pile running procedures described heretofore. As such, peak strengths are neglected, to confine the performance of each model primarily to stiffness effects. A uniform unit weight without depth dependencies was chosen based on a typical unit weight for marine clays (18 kN/m³), as informed by the given literature of the performed soil tests.

2.3. Large deformation model description

The CEL method has been widely implemented for offshore geotechnical applications involving large deformation, such as pile

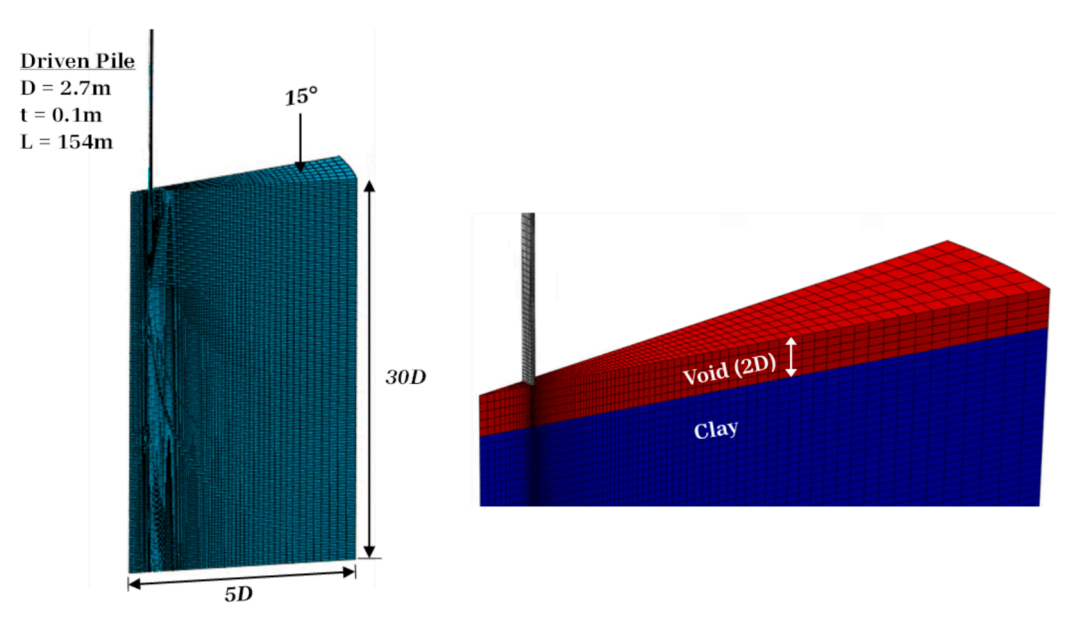


Fig. 3. Soil-pile geometry and Eulerian-Lagrangian mesh (left) full domain (right) neighbourhood surrounding the pile.

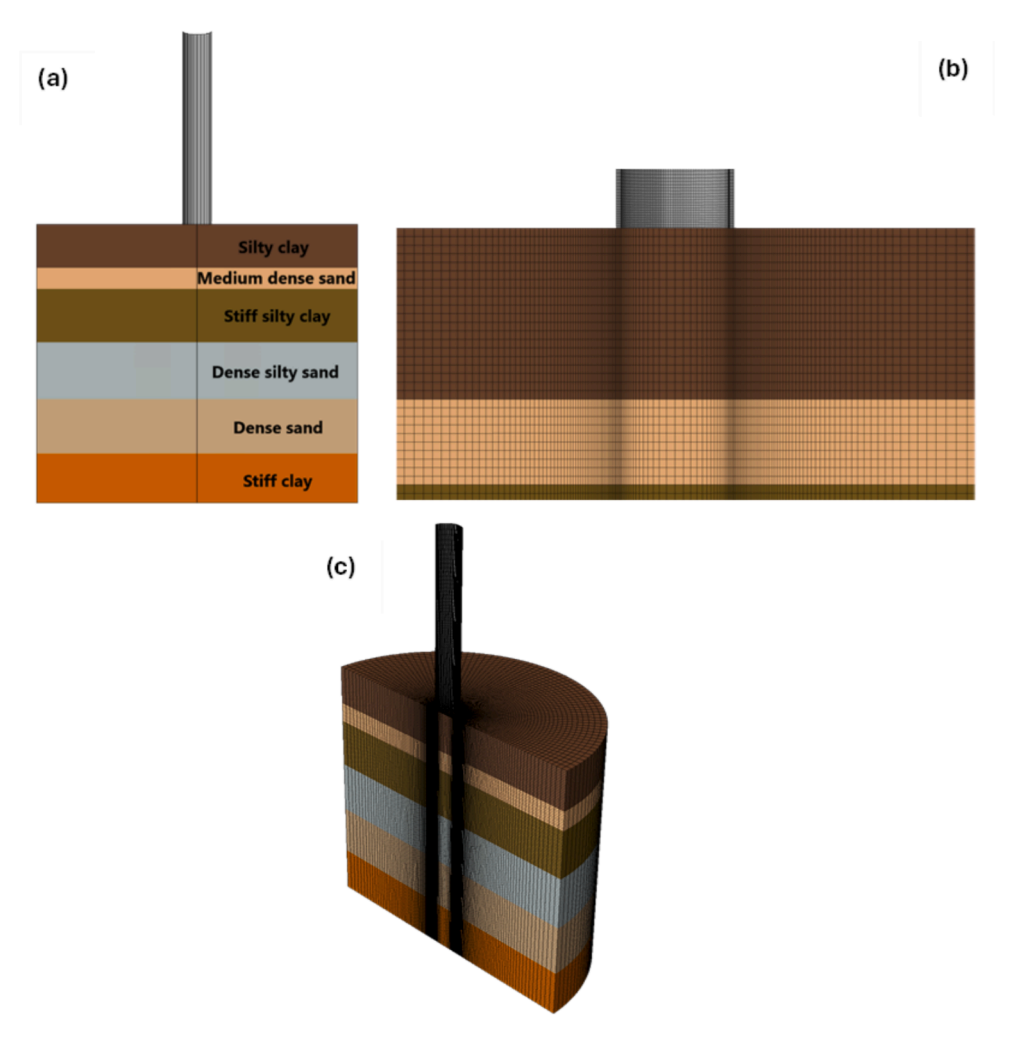


Fig. 4. Model geometry and layering (a) soil stratigraphy (b) mesh distribution surrounding the pile shaft (c) half-cylinder geometry.

installation (Fan et al., 2021; Hamann et al., 2015; Staubach et al., 2021). In this study, the method is applied using the commercial software Abaqus CAE (Dassault Systèmes, 2024). The process involves an Eulerian domain of fixed spatial nodes where materials (in this case soils) are allowed to flow through the mesh. This process circumvents solver convergence issues caused as a result of mesh distortion. Pile-soil interactions are controlled by a contact penalty algorithm, allowing Lagrangian objects (piles, in this study) to interact with Eulerian materials. The geometry of the pipe pile under consideration is based on previously published CEL pile run cases (Tian & Cassidy, 2022; Zhao et al., 2023), described by an outside diameter D = 2.7 m, wall thickness t = 0.1 m, length L = 158 m and submerged weight W = 643.9 t. This particular pile system refers to the Liwan3-1 foundation piles, which is one of the largest in the world, at a total length of 158 m, with a total penetration target of 135 m (Sun et al., 2022; Sun et al., 2018). Based on the size of this particular case, pile running poses a significant risk due to the excessive self-weight of the system. A 15° wedge representing 1/24 of the total soil-pile domain leverages the symmetry of the problem to reduce the computational requirements of the model (see Fig. 3). Both vertical and lateral axes were extended to a sufficient size to avoid boundary effects influencing the pile behaviour. Fine Eulerian elements were required in the region surrounding the pile tip and shaft to maintain accuracy and limit Eulerian leakage through the Lagrangian domain, as is a feature of CEL models with coarse elements or sharp angular contact surfaces. An initial 'void' layer equal to two pile diameters in thickness located at the mudline accommodates any pile heave during the pile run, providing sufficient space for uplift at the top of the Eulerian domain.

At the start of the analysis, initial geostatic stresses are balanced with gravity, with the pile given full fixities. The pile is placed at the seabed level, and the vertical restraint is removed thereafter to allow downward movement. As previously indicated, simplifications to the soil constitutive behaviour are focused on highlighting stiffness-based impacts for pile running. Further to this concept, the Eulerian soil domain considered herein consists of single-layered homogeneous clays, as opposed to those exhibiting depth-dependent behaviour. This is akin to typical "weightless soil" analyses where the shear strength is the primary contributing factor. For each given soil, a total stress Tresca criterion is used to model the clays of this study, with a Poisson's ratio ν of 0.49, to assume near-constant volume conditions emulating undrained behaviour. As per Mayne and Kulhawy (1982), the ratio between horizontal and vertical effective stress at rest (K_0) for lightly overconsolidated is assumed to be 0.9. An initial in-situ stage was implemented prior to the pile-running stage, based on the specified K_0 value. Thereafter, the sole model change in the pile running stage constituted the release of the pile vertical fixity, thereby permitting the pile to run under self-weight. As CEL does not permit displacement boundary conditions for the soil domain, soil flow is prevented by zero velocity boundary conditions to the sides of the model in the normal direction. At the base, zero velocity conditions were applied in all directions.

A pile running stage, simulating of 5 s of the pile running process was deemed sufficient in all cases to allow the pile to come to rest. Both nodal vertical displacements and velocities of the pile tip were extracted to assess the pile run. Similarly, plastic equivalent strains, Eulerian Volume

Table 2 Soil parameters in design — Source: (Sun et al., 2018).

	Stratum	Depth [m]	Unit weight [kN/m ³]	Undrained shear strength [kPa]	Sensitivity [-]	Internal friction angle [°]	Interface friction angle [°]
Layer							
1	Sand	0.0 - 3.0	17.9	_	_	25.0	16.7
2	Clay	3.0 - 11.1	18.3	27.5	4.0	_	_
3	Sand	11.1 - 14.0	18.6	_	_	34.0	20.0
4	Clay	14.0 - 18.0	18.6	50	4.0	_	_
5	Sand	18.0 - 20.0	18.1	_	_	33.0	20.0
6	Clay	20.0 - 25.0	18.5	50	4.0	_	_
7	Sand	25.0 - 30.3	19.1	_	_	30.0	20.0

Fractions (denoting the fraction of each element containing soil, as opposed to the pile), stress components and velocities were extracted for the soil domain at 200 regular time intervals across the pile run stage. In modelling the pile penetration behaviour, a general contact algorithm defined the interaction between Eulerian and Lagrangian domains. Interactions between the soil and the internal and external shaft surfaces, as well as the pile tip. The hard contact between the pile and the soil was set in the normal direction, based on a friction factor of $1/S_t$ of 0.5, as is commonly used (Xu et al., 2024). The pile domain is considered a rigid body in order to keep the computational costs low, with pile deformation beyond the scope of the present study. Undrained behaviour is assumed based on the sudden rapid, short-term loading rates of piles at velocities which are in some cases exceeding 10 m per second, combined with the low permeability of clay, such that pore pressures do not have sufficient time to dissipate. Finnie and Randolph (1994) presented a dimensionless velocity parameter $V = vd/c_h$, describing the drainage state of the soil, where v is the velocity of the object, d is the foundation diameter, and c_h is the coefficient of consolidation. Based on their findings, V > 10 constitutes undrained behaviour. Hence it is evident that for soils under loading due to pile running requires particularly a particularly large coefficient of consolidation to produce drained behaviour.

In the case of uncontrolled penetration of pipe piles in clay, the shaftsoil contact interface formulation is a primary factor in accurately defining the shaft resistance. CEL implements a Coulomb frictional model to calculate friction, as such, the maximum shear strength τ_{max} can be used to describe the soil-pile shear behaviour. Based on Equation (4), τ_{max} is defined based on the undrained shear strength of the soil (70 kPa) and the friction ratio α , i.e. the inverse of the soil sensitivity $1/S_t$, representing a fully remoulded state surrounding the pile during pile running which can be considered as a lower bound. An upper bound of $\alpha = 1$ (as required in Equation (4) provides an estimation of the soil-pile interface along the shaft with no degradation of skin friction. However, due to the negligible sensitivity of the clayey soils under consideration, the bounds on α provide minimal effect. An α value equal to unity is used for normally consolidated clays, with the lightly over consolidated clays considered in this work implement a slightly smaller, although comparable, value. Individual contact sets for the tip, internal and external shaft surfaces were defined to separate the contributions each component provides to the total resistance force. The ratio of internal to external skin friction β is given by 0.5 (as required in Equation (3), in alignment with Dover and Davidson (2007).

2.4. Model validation based on analytic formulation

In validating the CEL pile running model, the aforementioned analytic procedure was used based on the instrumented monitoring during the pile case in the South China Sea, outlined in both Sun et al. (2018) and Zhao et al. (2023). This constitutes a reproduction of the CEL model by Zhao et al. (2023), with equivalent results as is to be expected, given the use of the same model parameters, whose layering and model geometry are presented in Fig. 4. While the stratigraphy and soil parameters are provided in Table 2, all further model properties are consistent with the single layered clay model, Zhao et al. (2023). To provide a

Table 3
Analytical model inputs.

Property	Value
Ram weight [kg]	163,600
Pile weight [kg]	643,900
Coefficient of restitution [steel]	0.5
Ratio of internal to external skin friction [-]	0.5
Pile outer diameter [-]	2.743
Wall thickness [-]	0.1
Pile length [m]	158

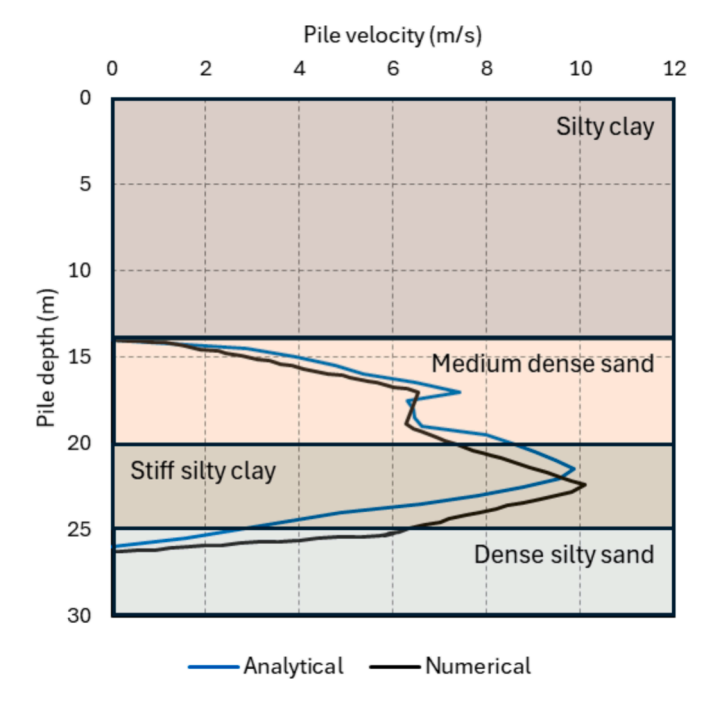


Fig. 5. Comparison of analytical and numerical models for an observed pile running case in the South China Sea.

suitable comparison, further model inputs are required for the analytical procedure (Table 3). A comparison of pile velocities with depth for both models are given in Fig. 5, providing strong agreement, albeit with slightly higher peak velocities observed in the analytical code (at depths of 16 and 22 m), with a shift in the depths where these values occur.

2.5. Contribution of elastic modulus in pile run analyses

Based on a uniform clay, pile penetration behaviour was considered for soils from Table 3 with varying stiffness, in addition to supplementary clays exhibiting higher stiffnesses ($E = 1000\&2000s_u$), the results of which are compared with the analytical solution given by Sun et al. (2022). Further validation is provided in terms of an identical CEL model of the case study described in (Zhao et al., 2023) (also conducted

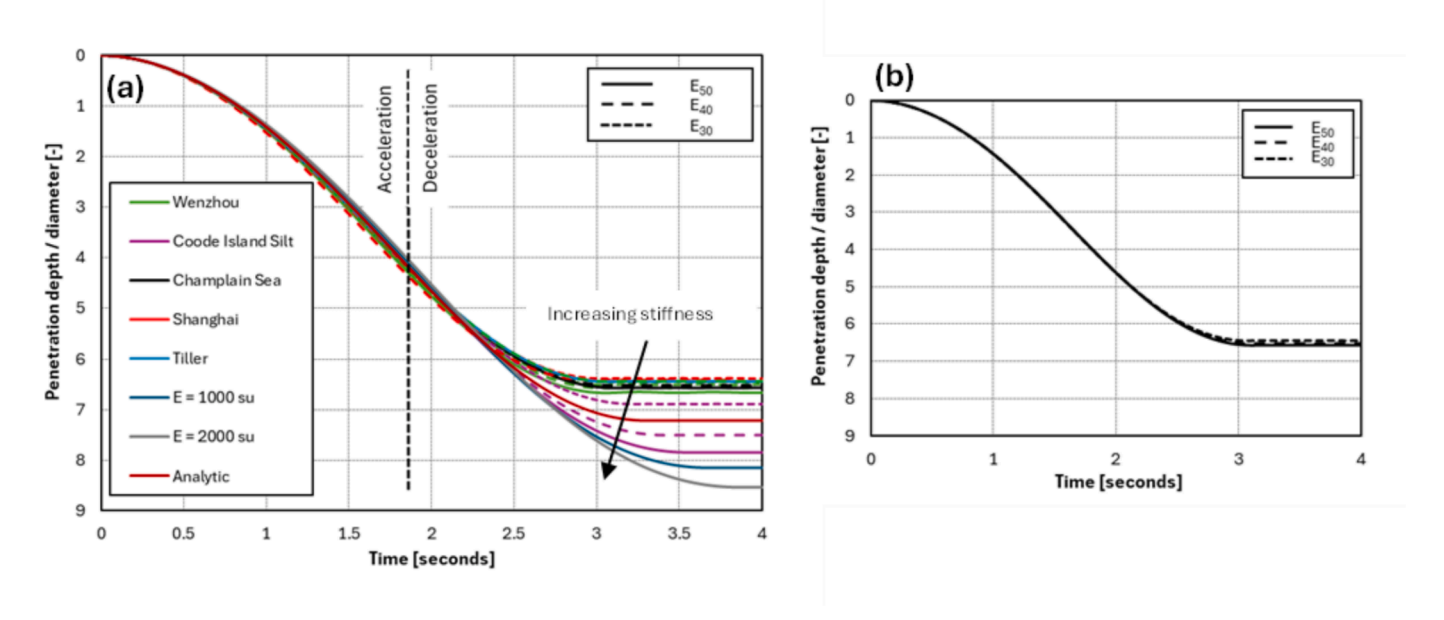


Fig. 6. Normalised pile penetration depth (a) penetration behaviour for various soils (b) penetration behaviour for Champlain Sea clay, $E_{30} - E_{50}$.

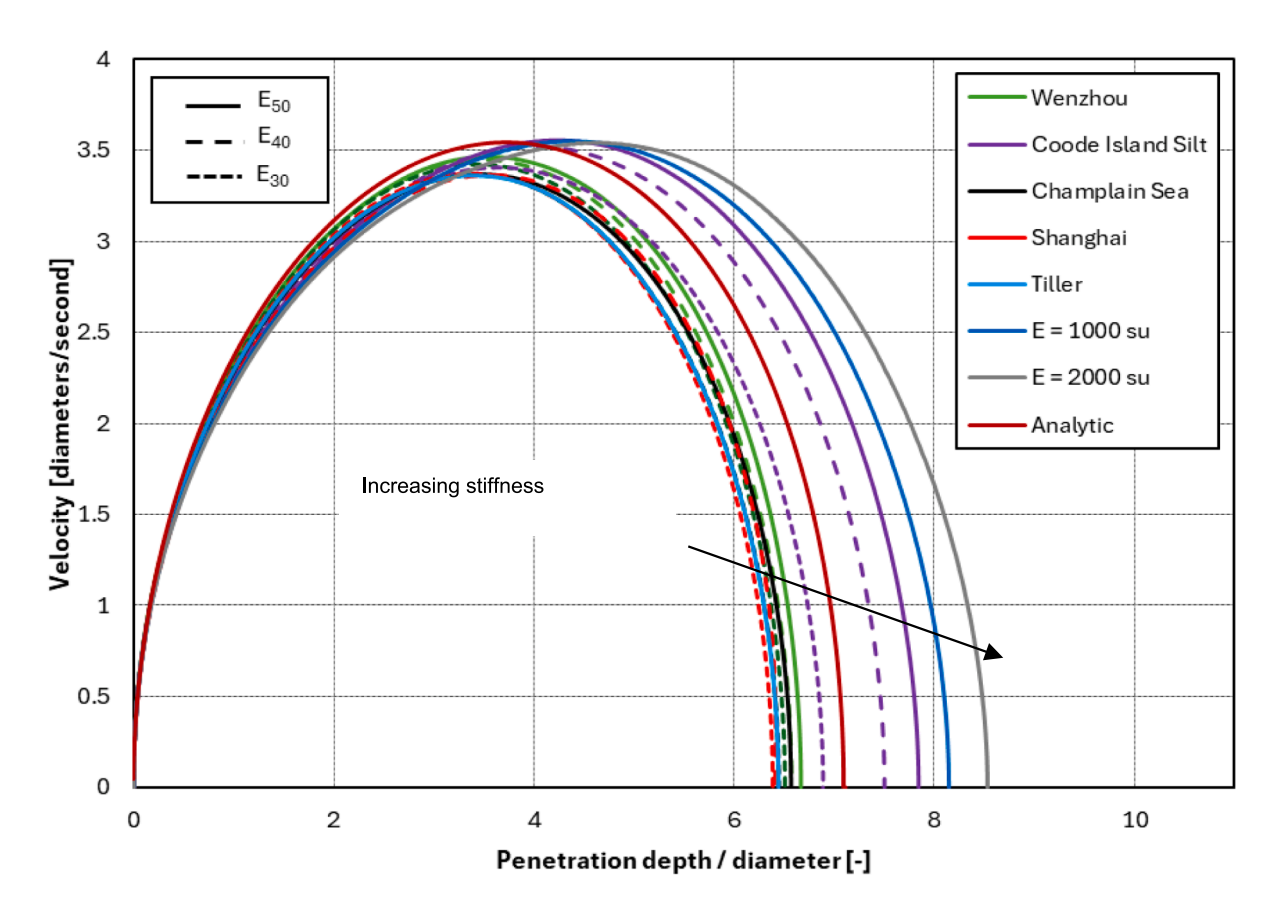


Fig. 7. Normalised pile velocity with depth.

using CEL), with the exact results obtained due to the common modelling approach. Normalised penetration profiles with time are given in Fig. 6, providing strong agreement with the analytical solution. When the pile driving force outweighs the resistive forces applied by the soil during the acceleration phase (t < 1.8s), penetration is relatively uniform for various soil stiffnesses. However, increases in the soil rigidity

prolong the pile descent and the period taken to come to rest. While this may seem counterintuitive, the role of stiffness on the size and shape of the plastic zone surrounding the pile is well known, as described herein. A final penetration depth of approximately 6—8 pile diameters is noted across the region of elastic moduli considered, where the pile run remains unaffected by the choice of E_{30} – E_{50} as is the case in Fig. 6(b)

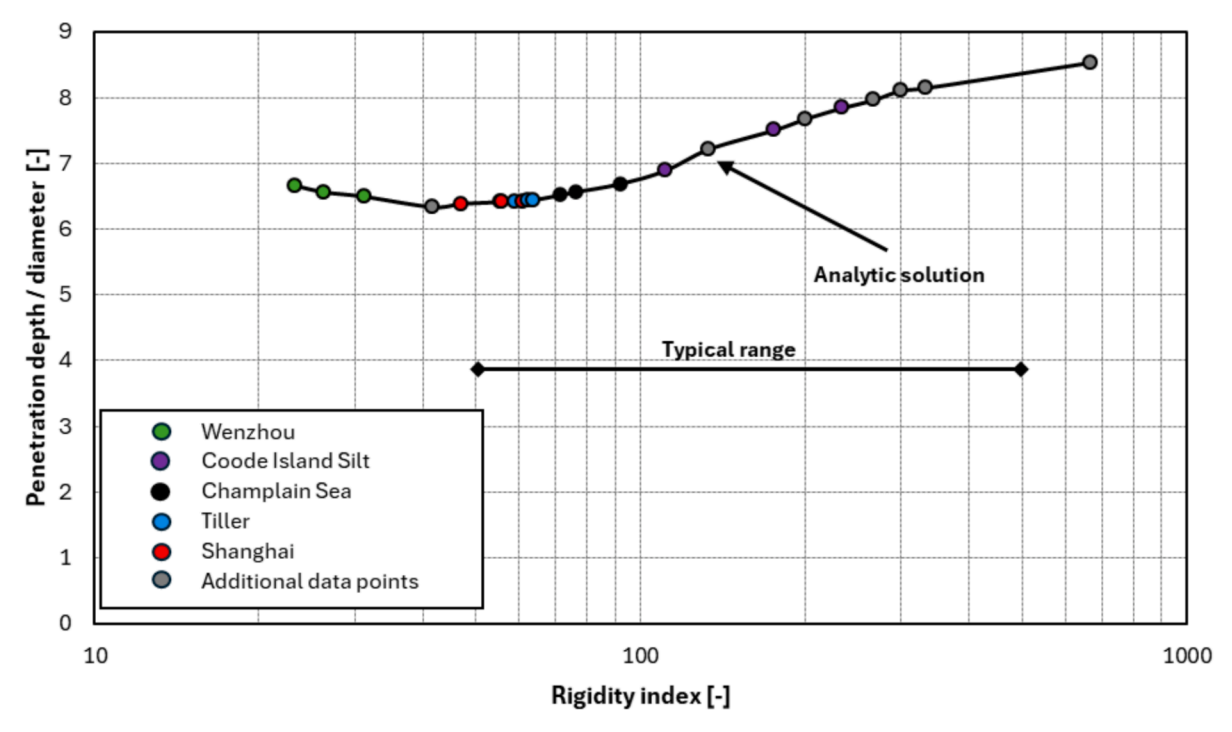


Fig. 8. Final penetration depth as a function of soil rigidity index.

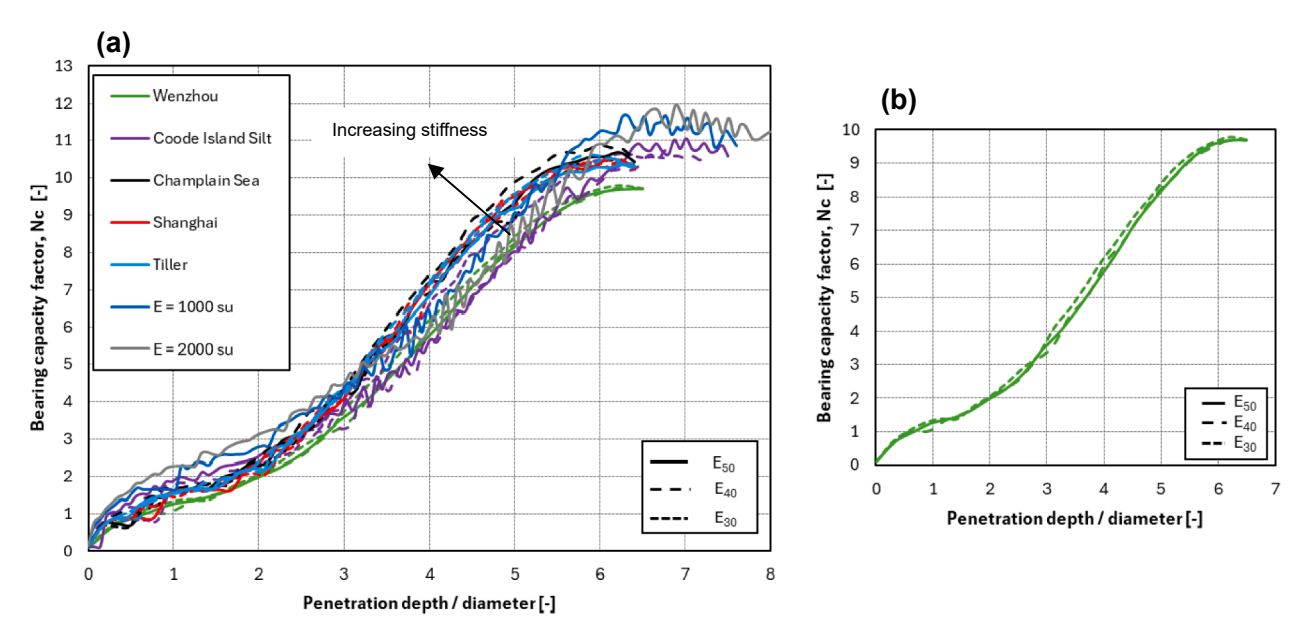


Fig. 9. Bearing capacity factor N_c with depth (a) penetration resistance for various soils (b) for Wenzhou clay, $E_{30} - E_{50}$.

which indicates the penetration profile for Champlain Sea clay. Coode Island Silt provides the exception due to a reasonable reduction in the secant modulus with shear strain.

The velocity of piles in uniform clay produces a parabolic arc when descent commences from the mudline (Fig. 7), as the majority of the soil resistance is derived from shaft resistance, and the shaft area is contact with the soil increases linearly with depth, this results in a second-order velocity profile. In the case of Wenzhou, Tiller and Shanghai clays, negligible differences in pile velocities and, therefore total pile displacement are noted, these being the softest of the clays considered. The total penetration depth as a function of soil rigidity is given in Fig. 8 over the typical range of soil rigidity (G = 50 - 500), with the analytical solution congruent with $I_r = 133$. Additional data points are provided to

reinforce the trend at high stiffnesses. When assessing the end tip resistance of driven piles with conventional bearing capacity theory, a bearing capacity factor in clay of $N_c=9$ is commonly used, constituting a soil rigidity index of $I_r=45.6$, or, in this case, an elastic modulus of 9.6 MPa, as derived from Equation (13). The bearing pressure with respect to depth is used to determine N_c , which does not stabilise until greater than 6 pile diameters of penetration (Fig. 9). As expected from conventional bearing capacity theory, the end-bearing resistance increases with stiffness, while the differences between expected N_c factors derived from Equation (13) are attributed to the depth required for the bearing capacity factor to achieve a steady state. This is echoed by Teh and Houlsby (1991), who noted that shallow penetration approaches are often inappropriate for deep bearing capacity theory. This is attributed

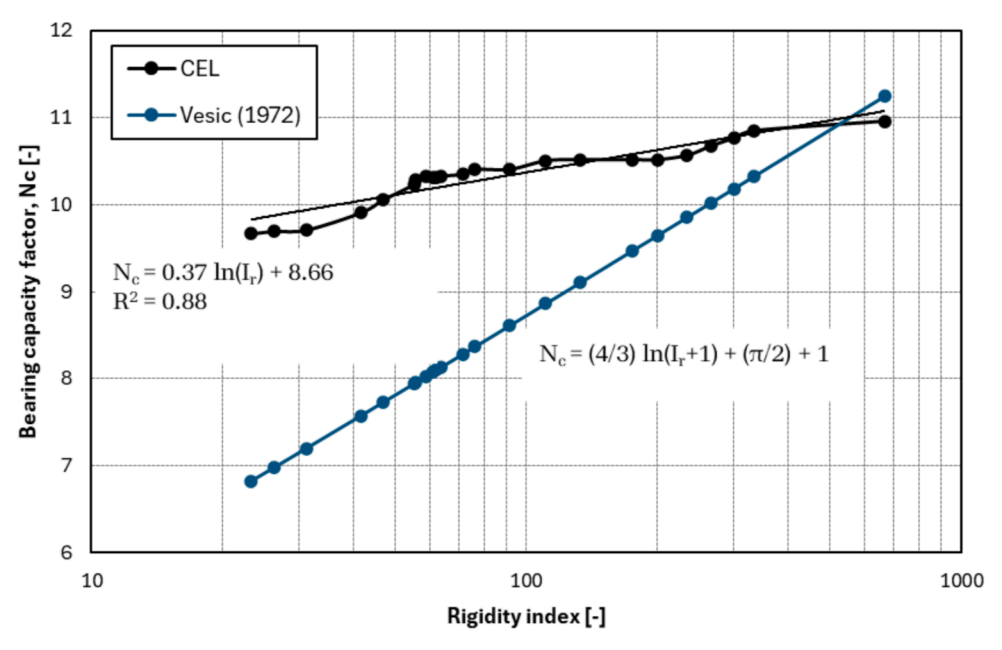


Fig. 10. Comparison of bearing capacity factor N_c from LDFE simulation with respect to Vesić (1972).

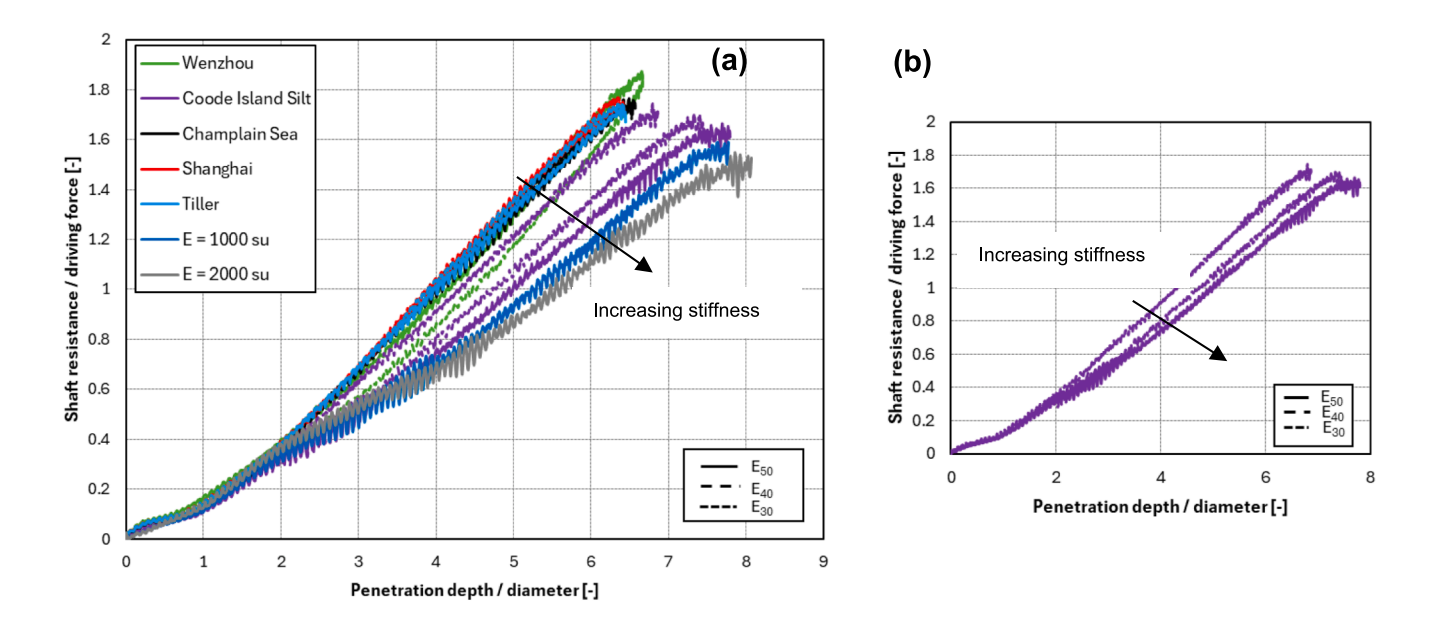


Fig. 11. Normalised shaft resistance for (a) various soils (b) Coode Island Silt, $E_{30}-E_{50}$.

to the transition from shallow to deep failure mechanisms that are confined to the region surrounding the penetrating object. Fig. 10 shows the difference between bearing capacity factors at a stable depth, which achieve parity at $I_r = 530$.

2.6. Contribution of shaft resistance

Similar to the end tip resistance, the total shaft resistance with depth is presented Fig. 11. With the shaft resistance providing the primary resistive force, the resistance is given as a ratio of the total driving force. As such, the trends observed in Figs. 6 and 7 are attributed to the decrease in shaft friction with respect to stiffness, whose contribution coincides with the commencement of the pile deceleration phase. A strong negative, linear trend can be seen between the total shaft resistance (combined internal and external surfaces) as the pile comes to rest

and the logarithm of the soil rigidity index Fig. 12. As per the contact definition, the ratio of internal and external skin friction is given $(\beta=0.5)$. As with the end tip bearing capacity factor, the ratio of the two components stabilises, in this case after two pile diameters of penetration, before which, the internal shaft friction is of similar scale to the external analogue (Fig. 13). The individual force contributions to the pile system (Fig. 14) indicate the external shaft resistance as a dominant factor, while the end tip resistance provides minimal contribution, as expected in clayey soils. When the sum of the resistive components outweighs the driving forces (as per the left-hand side of Equation (1), the pile decelerates until it comes to rest.

2.7. Dissipation of pile kinetic energy

The governing factors impacting the shaft resistance with respect to

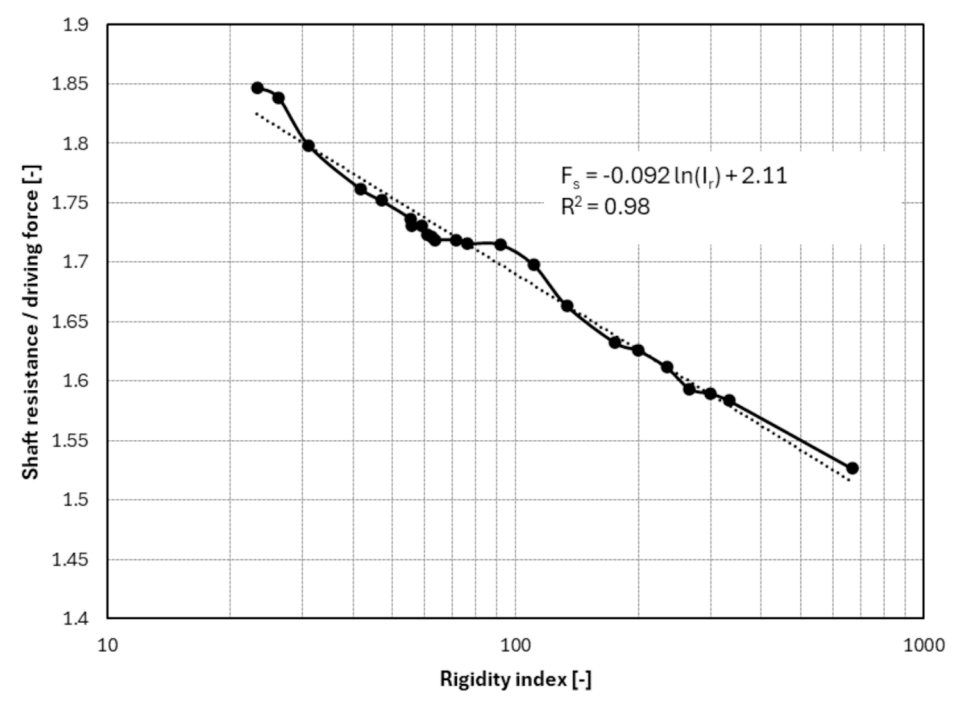


Fig. 12. Normalised total shaft resistance with respect to soil rigidity.

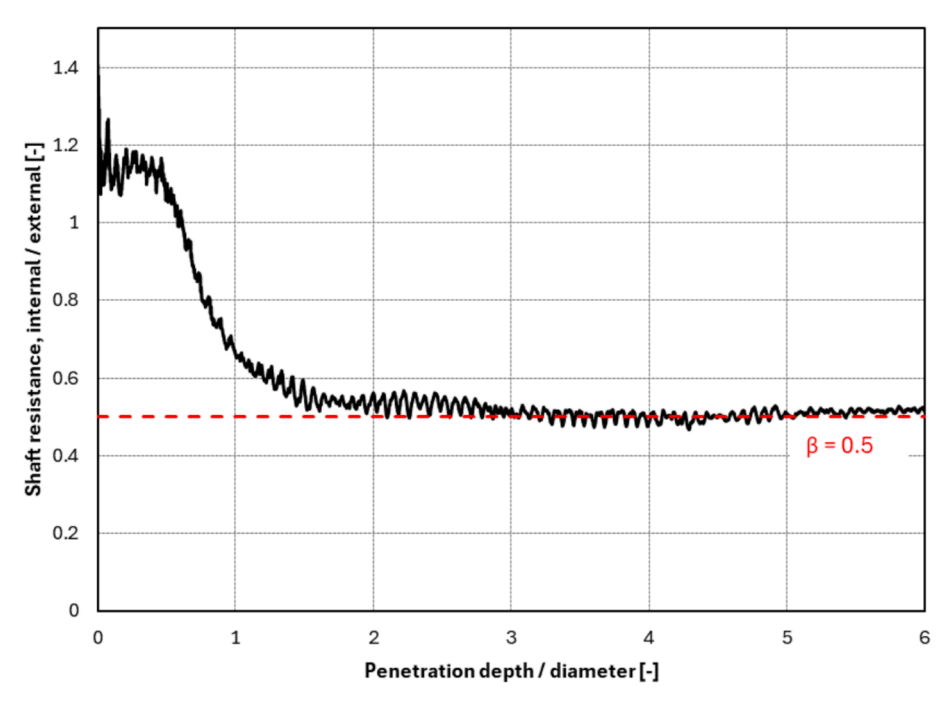


Fig. 13. Ratio of internal to external shaft resistance as a function of pile penetration.

elastic stiffness are best described as a function of the energy of pile-soil system. These are classified as elastic and inelastic strain energy, frictional dissipation and kinetic energy. Due to the compression and shear of the soil during the pile run, the pile kinetic energy is converted to elastic and inelastic strain energy as a function of the elastic modulus. Inelastic strains are associated with irreversible plastic deformation as a result of the pile run. Several choice soils are selected from Table 1 as further explanation of the evolution of the energy balance within the soil-pile system. As with Fig. 15(a), a reduced amount of kinetic energy is transferred to elastic strain energy as the elastic modulus increases. Due to the large-strain behaviour of the pile run, energy is primarily

transferred to plastic (inelastic) strain and friction, as shown in Fig. 15 (b)-(c). An increase in the plastic strain is a result of the increased plastic bulb surrounding the pile tip. While the stiffness of Champlain Sea clay and Coode Island Silt are dissimilar, the plastic and frictional dissipation is proportionate, as further highlighted by the comparative penetration behaviour (Fig. 8). As such, reduced plastic dissipation of Shanghai clay and a clay exhibiting an elastic modulus E=125su produces a shortened pile run. The overall kinetic energy of the system can be seen in Fig. 15 (d).

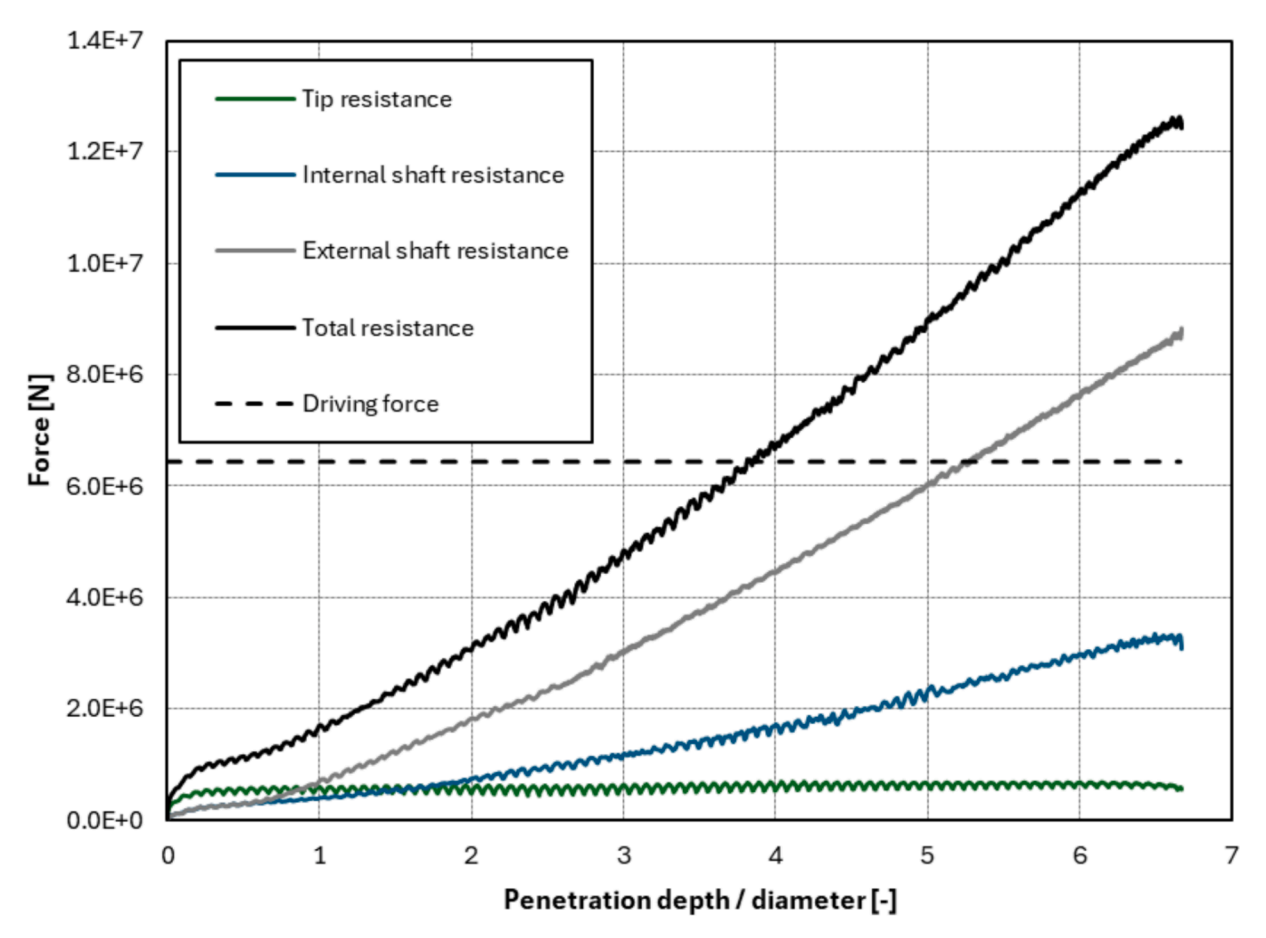


Fig. 14. Forces applied to the pipe pile during penetration.

2.8. Heave due to penetration

As the pile is driven, the soil enters the open end of the pile. Depending on the driving conditions and soil type, this soil may either flow out or form a soil plug. During the run, the penetration of the pile displaces surrounding soil, leading to upward movement of soil both internal and external to the pile. Cohesive soils such as clays are more prone to heave due to their plasticity and low internal resistance, as is also the case for large diameter piles. If the driving force is primarily transmitted to the pile tip (end-bearing), the soil inside the pile experiences greater resistance, contributing to heave, as is the case within the initial stages of the pile fall during the acceleration stage (as per Fig. 14). Thereafter, the pile decelerates with minimal impact on additional heave. As a result of the penetration process, varying degrees of soil heave at the ground surface within (and external to) the pipe pile occur, due to the near incompressible behaviour of the saturated, insensitive clays presented. Fig. 16 presents several typical snapshots of the vertical heave during the pile penetration process (with the model domain mirrored about the axis of symmetry for the purposes of visualisation). At first, vertical displacement of the soil is limited to the direct region surrounding the pile-soil contact surface. As the pile continues to accelerate, a partially plugged region within the pile is observed, exhibiting some arching, as is common for piles in fine grained soils (Jardine et al., 2005). As the pile continues to descend, further heave can be observed within the pile, however at a diminished rate. The degree to which heave at the mudline occurs is dependent on the rigidity index of the soil, with heave above 1 m within the pile column observed as the stiffness of the soil increases. Increased levels of heave are present for stiffer clays due to the increased penetration displacing additional soil both internal to and surrounding the pile. Equations (11) and (13) highlight the impact of rigidity index on the end bearing resistance of the pile, as the controlling factor in heave as shown in Fig. 17, with the logarithm of the rigidity index producing linear increases to N_c values. As such, greater stiffness produces increased heave internal to the pile.

No discernible heave is evident at lateral distances greater than 1 pile diameter from the shaft, external to the pile. Fig. 18 provides an indication of the increased stress bulb with additional stiffness (t = 0.3s), whose vertical dimension is seen to expand, in addition to minor lateral extensions. Prior to the commencement of pile running, a geostatic loading stage produces in-situ stresses based on the K_0 procedure. Thereafter, during loading, stresses applied to the soil by the pile running process form a combination of axial, radial and shear stresses. As pile penetration occurs, lateral soil movement compresses the soil surrounding the pile, with significant increases to radial stresses surrounding the shaft. Similarly, shear stresses develop throughout the pile running process due to the friction and adhesion of the interface between the pile shaft and the surrounding clay. Shear stresses surrounding the pile result in plastic deformations, as given by the stress bulbs in Fig. 18. These bulbs increase in size with increasing stiffness, extending downwards from the base of the pile. Stiffer soils transfer loads more directly downward because they resist lateral deformation and tend to distribute stress in a more concentrated manner. The base of the shaft is primarily affected by axial forces parallel, compressing the soil beneath the pile tip while also controlling the upward flow of soil within the pile.

3. Implications for analytic method

Based on the strong linear relationship between shaft resistance and the logarithm of soil rigidity, the aforementioned analytic method is adjusted to provide greater accuracy. Modifications are limited to the shaft resistance, with no changes to the end tip resistance, due to the penetration depth required for the bearing capacity factor N_c to reach a

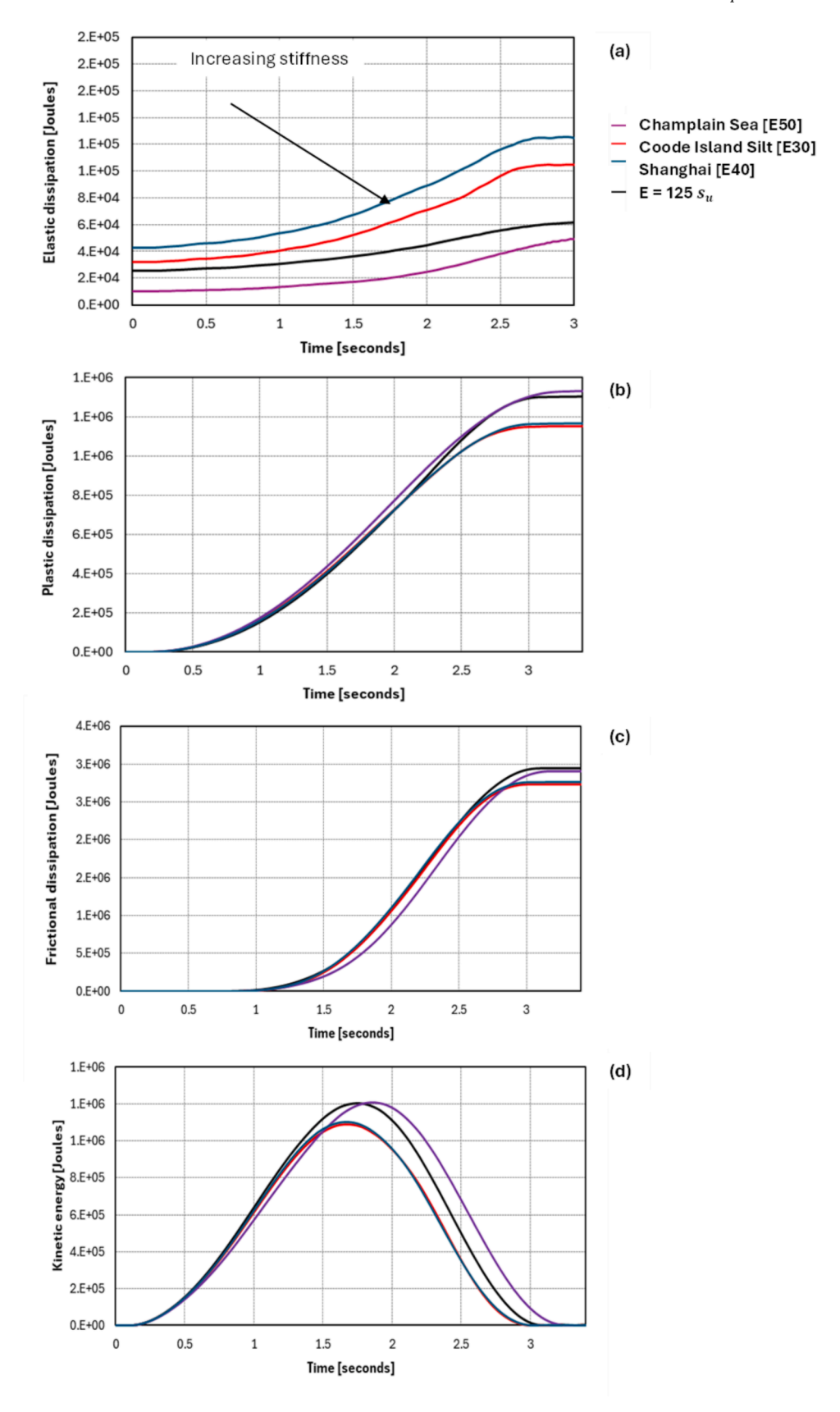


Fig. 15. Energy components (a) elastic dissipation (b) plastic dissipation (c) frictional dissipation (d) kinetic energy.

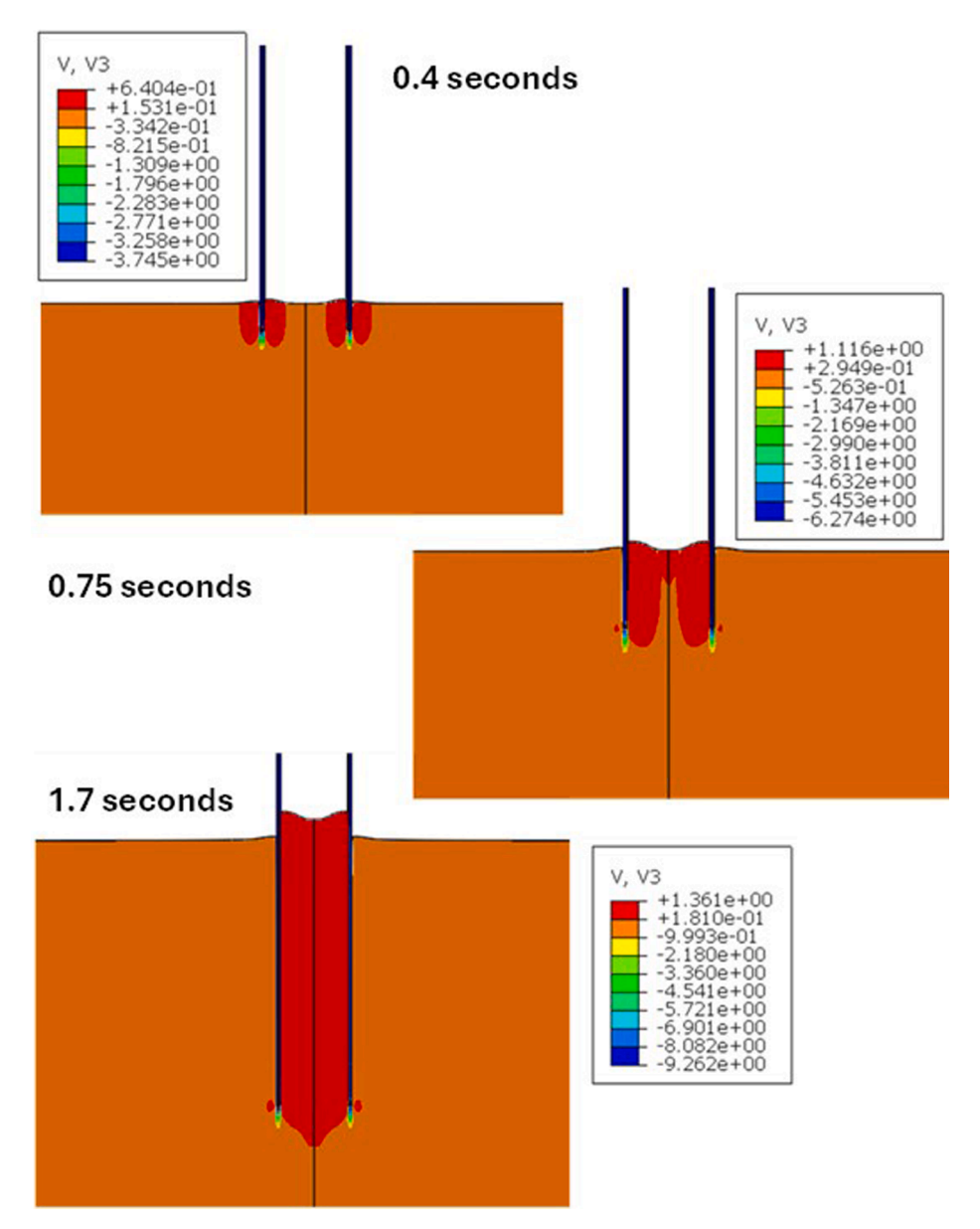


Fig. 16. Typical mudline heave profile during pile penetration.

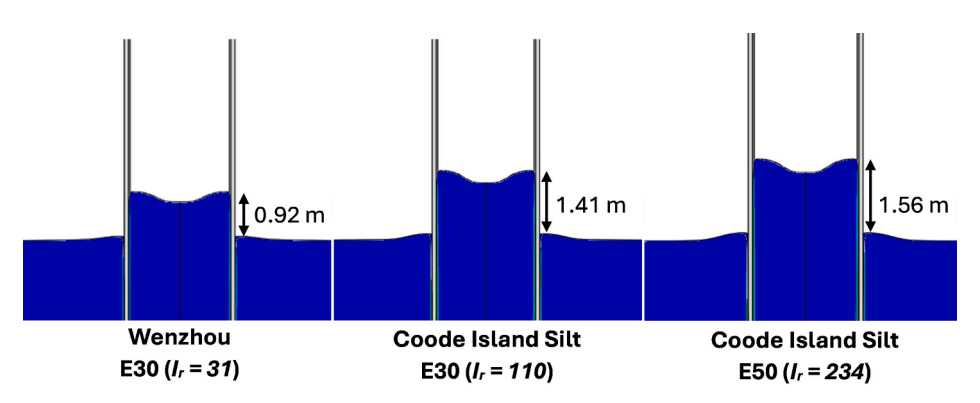


Fig. 17. Heave as a result of varying soil rigidity.

steady state. As per ISO standards, the shaft resistance given in Equation (4) can be combined with the fitted trend given in Fig. 8 to create an updated α factor as follows

$$\alpha = \frac{G_{pile}}{s_u} (2.11 - 0.092 \ln I_r) \tag{15}$$

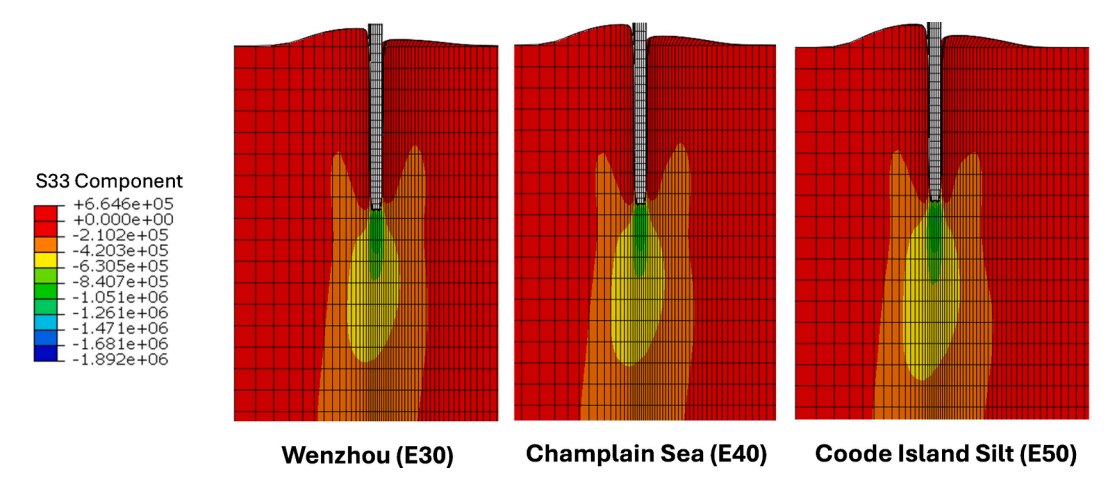


Fig. 18. Increasing stress bulb with additional stiffness (t = 0.3s).

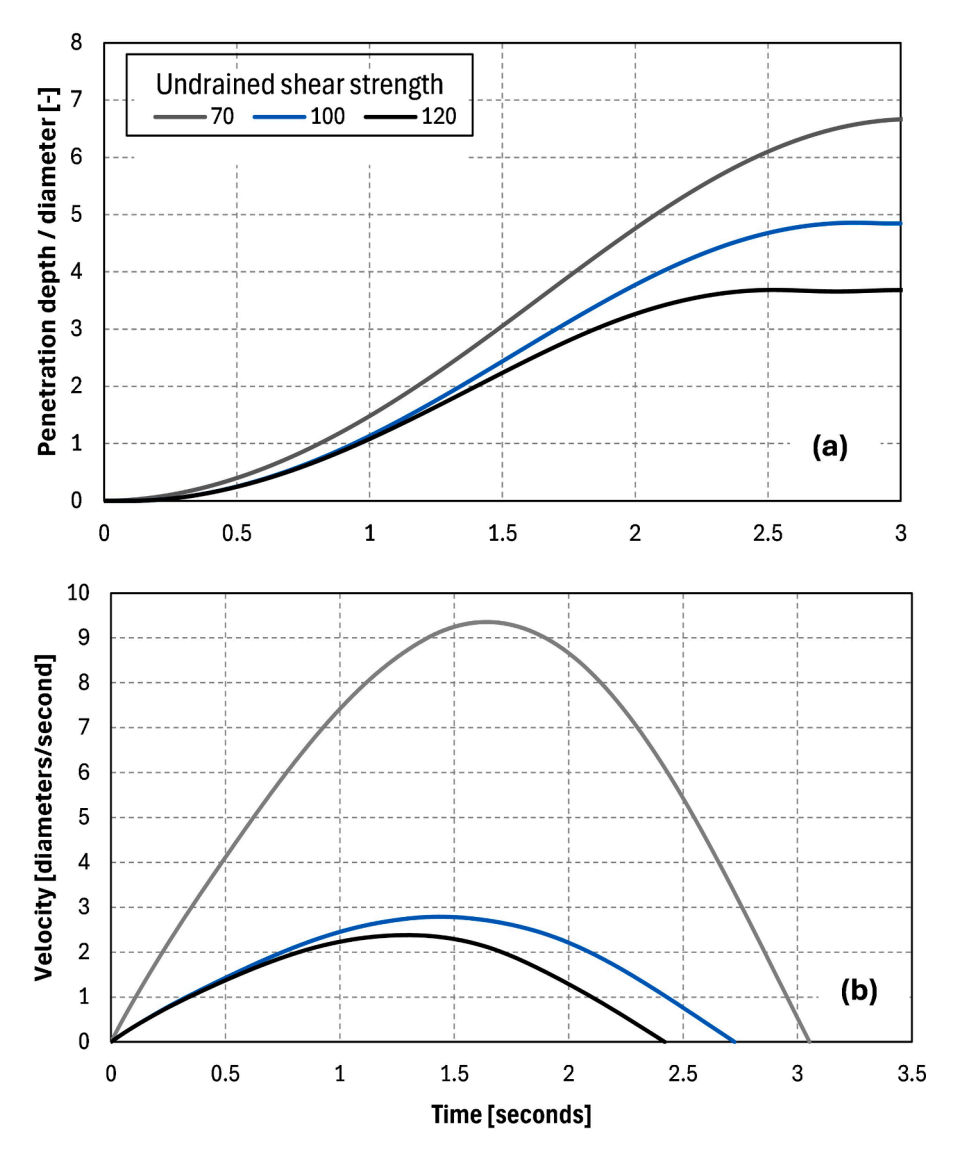


Fig. 19. LDFE penetration behaviour for various s_u (a) normalised depth (b) normalised velocity.

such that α contains a weight force term and a stiffness term. The applicability of this equation is considered for further simulations with additional values of s_u (100 and 120 kPa). Fig. 19 shows the pile displacement and velocity profiles for these undrained shear strengths

(Wenzhou E_{50}) from CEL simulation. In the case of $s_u = 120kPa$ (an increase of 70 % s_u compared to the base-model of 70 kPa), the penetration depth is reduced by almost half. The performance of the modified analytic code for various elastic moduli is compared with the LDFE

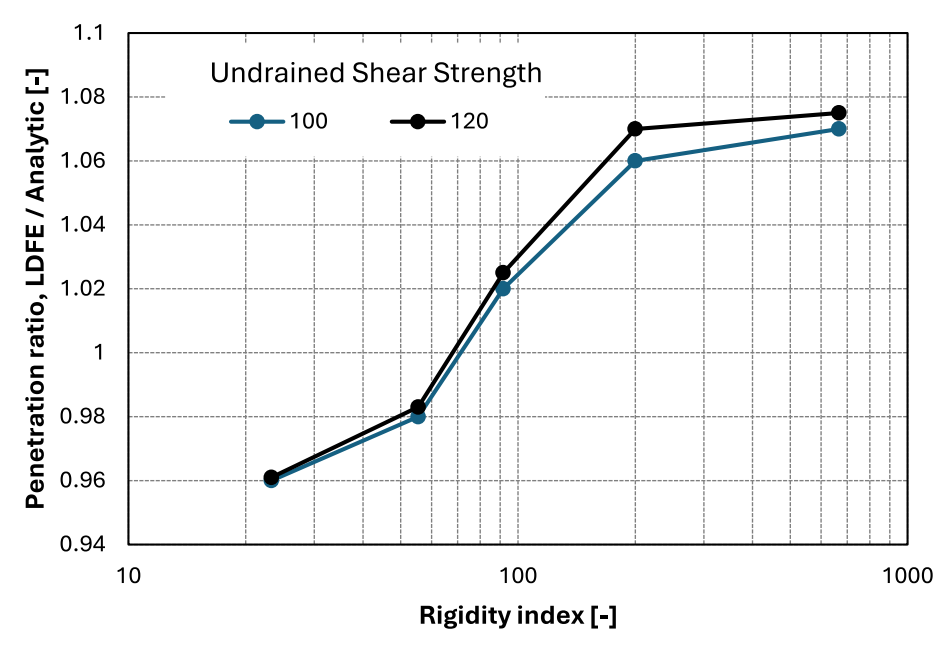


Fig. 20. Comparison of penetration behaviour for the modified analytic method and LDFE (Tiller clay).

simulated pile run in terms of both the penetration depth and velocity. Fig. 20 shows the penetration ratio (LDFE / analytic) for Tiller clay, showing strong agreement. The penetration behaviour of the two methods differs by a maximum of 8 % for high stiffnesses, where the greatest penetration depths are observed. While stronger agreement is noted for $120~\mathrm{kPa}$ clay than for the $100~\mathrm{kPa}$ case, this is attributed to the reduced variation in penetration depths as the strength of the soil increases.

4. Conclusions

This paper presents a comparative study of five well-investigated fine-grained soils, whereby the uncontrolled pile penetration behaviour of a large diameter long pipe pile is considered using large deformation numerical simulation. Due to the varying stiffnesses of each clay, pile penetration depths were assessed based on a simplified linear elastic perfectly plastic criterion. As a result, an analytic procedure is modified to incorporate stiffness effects for determining penetration depths and velocities. Several conclusions can be drawn as follows.

- Over a typical range of the soil rigidity index, piles are capable of varying in final penetration depths in the order of two pile diameters due to the varying soil stiffness.
- (2) Considering the end bearing capacity of piles using CEL, the steady state bearing capacity factor N_c requires several pile diameters to reach a steady state. As such, the use of Vesic's stiffness-dependent bearing capacity factors do not provide strong agreement with those derived from large deformation simulation.
- (3) With increasing stiffness, a reduction in shaft resistance is observed due to the dissipation of elastic and inelastic energy, in addition to frictional dissipation. This results in a larger stress bulb surrounding the pile tip. A linear trend between the penetration depth and the natural logarithm of rigidity index is noted.
- (4) Due to increased penetration depths of piles with increased elastic modulus, greater heave at the mudline is observed due to additional soil being displaced.
- (5) Based on LDFE results, a modified analytic procedure is capable of accommodating stiffness effects to pile velocities and penetration depths with strong agreement. While limitations remain in terms of the capability of the analytic method to assess soil

flow, uplift and size of the plastic bulb, the technique provides an update to existing methods for greater accuracy.

CRediT authorship contribution statement

A.P. Dyson: Writing – original draft, Visualization, Validation, Investigation, Formal analysis. **A. Tolooiyan:** Writing – review & editing, Supervision, Methodology, Investigation, Formal analysis, Conceptualization. **K. Gavin:** Writing – review & editing, Investigation, Conceptualization.

Declaration of competing interest

The authors declare that they have no known competing financial interests or personal relationships that could have appeared to influence the work reported in this paper.

Data availability

Data will be made available on request.

References

API. (2020). API RP 2A-WSD: Planning, Designing and Constructing Fixed Offshore Platforms - Working Stress Design.

Baligh, M.M., Ladd, C.C., Vivatrat, V., 1980. Cone penetration in soil profiling. J. Geotech. Eng. Div. 106 (4), 447–461.

Chow, S., O'Loughlin, C., Goh, C., McIlduff, R., White, D., Chow, F., 2023. A comparative field study of free-fall cone and sphere penetrometers in soft sediment. Ocean Eng. 280, 114094.

D'Ignazio, M., Länsivaara, T., 2015. Shear bands in soft clays: strain-softening behavior in finite element method. Rakenteiden mekaniikka 48 (1), 83–98.

Dassault Systèmes. (2024). Abaqus/CAE, Version 2024. https://www.3ds.com.
Dover, A., & Davidson, J. (2007). Large Diameter Steel Pipe Piles Running under Self Weight in Soft Clay: Predicted vs. Observed Behavior—Richmond San-Rafael Bridge Seismic Retrofit. In: Ports 2007: 30 Years of Sharing Ideas: 1977-2007 (pp. 1-10).

 Fallah, S., Gavin, K., Jalilvand, S., 2016. Numerical modelling of cone penetration test in clay using coupled Eulerian Lagrangian method. Proc. Civ. Eng. Res. Ireland 29–30.
 Fan, S., Bienen, B., Randolph, M.F., 2021. Effects of monopile installation on subsequent lateral response in sand. I: Pile installation. J. Geotech. Geoenviron. Eng. 147 (5), 04021021.

Finnie, I., & Randolph, M. (1994). Punch-through and liquefaction induced failure of shallow foundations on calcareous sediments. Punch-through and liquefaction induced failure of shallow foundations on calcareous sediments.

- Hamann, T., Qiu, G., Grabe, J., 2015. Application of a Coupled Eulerian-Lagrangian approach on pile installation problems under partially drained conditions. Comput. Geotech. 63, 279–290.
- Hong, Z., Shen, S., Deng, Y., Negami, T., 2007. Loss of soil structure for natural sedimentary clays. Proc. Inst. Civ. Eng.-Geotech. Eng. 160 (3), 153–159.
- Jamali, H., Tolooiyan, A., Dehghani, M., Asakereh, A., Kalantari, B., 2018a. Long-term dynamic behaviour of Coode Island Silt (CIS) containing different sand content. Appl. Ocean Res. 73, 59–69.
- Jamali, H., Tolooiyan, A., Dehghani, M., Asakereh, A., Kalantari, B., 2018b. Post-long-term cyclic behaviour of Coode Island Silt (CIS) containing different sand content. Appl. Ocean Res. 80, 11–23.
- Jardine, R., Chow, F., Overy, R., & Standing, J. (2005). ICP design methods for driven piles in sands and clays (Vol. 112). Thomas Telford London.
- Kong, D., Deng, M., Xu, Y., 2019. Study on calculation of pile sliding interval of largediameter steel pipe piles on offshore platforms. Math. Probl. Eng. 2019 (1), 3549296.
- Liu, J., Afroz, M., Ahmad, A., 2021. Experimental investigation of the impact of salinity on Champlain Sea clay. Marine Georesour. Geotechnol. 39 (4), 494–504.
- Lu, Q., Randolph, M., Hu, Y., Bugarski, I., 2004. A numerical study of cone penetration in clay. Geotechnique 54 (4), 257–267.
- Lunne, T., & Andersen, K. H. (2007). Soft clay shear strength parameters for deepwater geotechnical design. SUT Offshore Site Investigation and Geotechnics.
- Lunne, T., Andersen, K.H., Low, H.E., Randolph, M.F., Sjursen, M., 2011. Guidelines for offshore in situ testing and interpretation in deepwater soft clays. Can. Geotech. J. 48 (4), 543–556.
- Mayne, P. (1995). Application of G/Gmax modulus degradation to foundation settlement analyses. Proc. US-Taiwan Workshop on Geotech.
- Mayne, P.W., Kulhawy, F.H., 1982. Ko-OCR relationships in soil. J. Geotech. Eng. Div. 108 (6), 851–872.
- Menard, L. (1957). Mesures in situ des propriétés physiques des sols.
- O'Loughlin, C., Blake, A., Gaudin, C., 2016. Towards a simple design procedure for dynamically embedded plate anchors. Geotechnique 66 (9), 741–753.
- Poulos, H., Carter, J., & Small, J. (2002). Foundations and retaining structures-research and practice. Proceedings of the International Conference on Soil Mechanics and Geotechnical Engineering.
- Poulos, H.G., 1994. Settlement prediction for driven piles and pile groups. Vertical Horizontal Deformations Found. Embankments.
- Randolph, M., Dolwin, R., Beck, R., 1994. Design of driven piles in sand. Geotechnique 44 (3), 427–448.
- Senders, M., Banimahd, M., Zhang, T., Lane, A., 2013. Piled foundations on the north west shelf. Australian Geomech. J. 48, 149–160.
- Sha, S., Dyson, A.P., Kefayati, G., Tolooiyan, A., 2023. Simulation of debris flow-barrier interaction using the smoothed particle hydrodynamics and coupled Eulerian Lagrangian methods. Finite Elem. Anal. Des. 214, 103864.
- Shengchang, G., Shaolin, W., 2011. Problems of rapid pile sinking during pile driving and solutions. Port Waterway Eng. 12 (12), 78–82.

- Staubach, P., Machaček, J., Skowronek, J., Wichtmann, T., 2021. Vibratory pile driving in water-saturated sand: Back-analysis of model tests using a hydro-mechanically coupled CEL method. Soils Found. 61 (1), 144–159.
- Sun, L., Jia, T., Yan, S., Guo, W., Ren, Y., Lei, Z., 2016. Prediction of pile running during the driving process of large diameter pipe piles. Ocean Eng. 128, 48–57. https://doi. org/10.1016/j.oceaneng.2016.10.023.
- Sun, L., Shi, J., Zhang, Y., Feng, X., Tian, Y., Wang, R., 2022. Analytical method for predicting pile running during driving. Appl. Ocean Res. 125, 103234.
- Sun, L., Wang, Y., Guo, W., Yan, S., Chu, J., Liu, X., 2018. Case study on pile running during the driving process of large-diameter pipe piles. Marine Georesour. Geotechnol. 36 (6), 709–721.
- Tatnell, L., Dyson, A.P., Tolooiyan, A., 2021. Coupled Eulerian-Lagrangian simulation of a modified direct shear apparatus for the measurement of residual shear strengths. J. Rock Mech. Geotech. Eng. 13 (5), 1113–1123.
- Teh, C., Houlsby, G., 1991. An analytical study of the cone penetration test in clay. Geotechnique 41 (1), 17–34.
- Tian, Y., & Cassidy, M. (2022). Pile Running Problem and Large Deformation Modelling. 20th International Conference on Soil Mechanics and Geotechnical Engineering, Sydney.
- Tolooiyan, A., Gavin, K., Dyson, A.P., 2024. Penetration of unconventional spudcan foundations using back analyses of large deformation CPT profiles. Ocean Eng. 304, 117563.
- Vesic, A.S., 1977. Design of pile foundations. NCHRP Synthesis Highway Practice 42.
 Vesić, A.S., 1972. Expansion of cavities in infinite soil mass. J. Soil Mech. Found. Div. 98
 (3), 265–290.
- Vesić, A.S., 1973. Analysis of ultimate loads of shallow foundations. J. Soil Mech. Found. Div. 99 (1), 45–73.
- Wang, J., Guo, L., Cai, Y., Xu, C., Gu, C., 2013. Strain and pore pressure development on soft marine clay in triaxial tests with a large number of cycles. Ocean Eng. 74, 125–132.
- Xu, S.J., Wang, Z., Yi, J.T., Liu, F., Tang, H.Y., Yin, S., 2024. Evaluation of existing pile responses to adjacent pile penetration: a novel passive P-δ curve approach. Comput. Geotech. 176, 106702.
- Yan, S., Jia, Z., Liu, W., Li, J., 2015. Reserch on the large diameter and supper long pile running under self-weight in the ocean engineering. J. Coastal Res. 73, 809–814.
- Ye, G.-L., Ye, B., 2016. Investigation of the overconsolidation and structural behavior of Shanghai clays by element testing and constitutive modeling. Undergr. Space 1 (1), 62–77.
- Yu, H., Mitchell, J., 1998. Analysis of cone resistance: review of methods. J. Geotech. Geoenviron. Eng. 124 (2), 140–149.
- Zhao, H., Wang, L., Sun, L.-Q., Tian, Y.-H., Reul, O., Chen, Q.-Z., 2023. Pile running in layered soils. China Ocean Eng. 37 (5), 829–841.
- Zhou, S., Zhang, W., Osman, A.S., 2024. Effect of soil stiffness on end bearing resistance of foundations in clay from large deformation numerical modelling. Comput. Geotech. 173, 106515.